Available online at www.sciencedirect.com

ScienceDirect

Geochimica et Cosmochimica Acta 325 (2022) 316–332

Geochimica et Cosmochimica Acta

www.elsevier.com/locate/gca

Kinetic controls on Sc distribution in diopside and geochemical behavior of Sc in magmatic systems

Zhen-Chao Wang [a], Mei-Fu Zhou [b,c,*], Martin Yan Hei Li [a], Paul T. Robinson [a,c], Daniel E. Harlov [c,d,e]

[a] Department of Earth Sciences, The University of Hong Kong, Hong Kong, China
[b] State Key Laboratory of Ore Deposit Geochemistry, Institute of Geochemistry, Chinese Academy of Sciences, Guiyang 550081, China
[c] School of Earth Resources, China University of Geosciences, 430074 Wuhan, China
[d] Deutsches GeoforschungsZentrum – GFZ, Telegrafenberg, 14473 Potsdam, Germany
[e] Department of Geology, University of Johannesburg P.O. Box 524, Auckland Park, 2006, South Africa

Received 25 October 2021; accepted in revised form 12 March 2022; Available online 18 March 2022

Abstract

Scandium is important in modern technology and is regarded as a strategic metal in many countries. It is highly dispersed in Earth's crust and rarely forms independent minerals. Clinopyroxene is the most important Sc-bearing mineral in some world-class deposits hosted in mafic–ultramafic intrusions, which are also the major source of laterite-hosted Sc deposits. However, the factors controlling Sc distribution in minerals have been little explored, impeding the understanding of the geochemical behavior of Sc and why it is common in some clinopyroxene grains. The newly discovered Mouding Sc deposit in SW China is hosted in a zoned intrusion composed, from core to rim, of monzogabbro, syenogabbro, gabbro, magnetite clinopyroxenite, and clinopyroxenite. Clinopyroxene in the intrusion is diopsidic in composition with high Sc contents (80–105 ppm). In-situ trace element mappings of diopside crystals reveal homogeneous, zoned, swallow-tailed, and hourglass internal Sc distribution patterns. These patterns can be produced through kinetically controlled incorporation of Sc on different crystal faces. The preferential substitution of Sc can take place on the {1 0 0}, {1 1 0} and {0 1 0} prism faces because of the high flexibility of the octahedral M1 protosites. The fast growth of diopside, which facilitates kinetically controlled crystallization, is dominated by textural coarsening and promoted by the hydrous parental magmas with low viscosities and active convection. The active flow and efficient interstitial communication of the magma can direct compatible elements from the magma into clinopyroxene, thus favoring formation of Sc-rich grains. Our study provides a feasible way to study intra-grain variations of Sc in minerals and emphasizes that kinetic effects may play a critical role in Sc distribution and enrichment in hydrous magmatic Sc deposits. We also show that disequilibrium crystallization may be more pervasive than previously thought, and the hourglass zoning of clinopyroxene can provide valuable information on this process.

Keywords: Clinopyroxene; Scandium geochemistry; Kinetic growth; Protosite flexibility; Textural coarsening

1. INTRODUCTION

Scandium is an important metal for production of solid oxide fuel cells and as a superalloy in automobiles and space vehicles. It has been regarded as a strategic metal in many countries because of the very low production rate worldwide (10–15 tons per year, Chakhmouradian et al.,

* Corresponding author at: State Key Laboratory of Ore Deposit Geochemistry, Institute of Geochemistry, Chinese Academy of Sciences, Guiyang 550081, China.
E-mail address: zhoumeifu@hotmail.com (M.-F. Zhou).

https://doi.org/10.1016/j.gca.2022.03.016
0016-7037/

2015; Williams-Jones and Vasyukova, 2018). In nature, many metals with lower abundances than Sc, e.g., Pb, Mo, Sb, and Au, form independent deposits, whereas Sc, as one of the 36 most abundant elements in the crust (Wedepohl, 1995), is highly dispersed and rarely concentrated sufficiently to form economic deposits. Sc-rich minerals, thortveitite [$(Sc,Y)_2Si_2O_7$] and bazzite [$Be_3(Sc,Al)_2Si_6O_{18}$] in pegmatites, have formerly been mined as by-products (Wang et al., 2021), but these sources are insufficient to meet modern demands. Currently, Sc-rich magmatic intrusions, including Alaskan-type mafic–ultramafic intrusions, ferrodiorite and ferrosyenite, are estimated to host most of the global Sc reserves (Daigle, 2017; Halkoaho et al., 2020; Wang et al., 2021). Such bodies can also be the source of Sc in world-class, laterite-hosted deposits (Chassé et al., 2017, 2019). Understanding the geochemical behavior of Sc in magmatic processes is therefore important for understanding the metallogenesis of Sc deposits.

Although classified as a rare earth element (REE), Sc has a much smaller radius (0.87 Å, VIII Sc^{3+}) than the other REEs (1.16–0.97 Å) (Shannon, 1976) and is not common in REE deposits (Williams-Jones and Vasyukova, 2018). In some circumstances, Sc is closely associated with minerals containing Fe, Mg, and high field strength elements (HFSEs) (e.g., Kempe and Wolf, 2006; Kalashnikov et al., 2016), such as clinopyroxene (median value ~60 ppm), amphibole (~48 ppm), garnet (~115 ppm) (Samson and Chassé, 2016; Chassé et al., 2018) and some HFSEs-bearing minerals, such as baddeleyite, columbite, ilmenite, wolframite, and cassiterite (Wise et al, 1998; Kempe and Wolf, 2006; Kalashnikov et al., 2016). Among these minerals, clinopyroxene is the most common and abundant, especially in mafic–ultramafic intrusions. However, the mechanisms controlling Sc enrichment in clinopyroxene cumulates are poorly understood and the large variations in concentration of clinopyroxene in ultramafic rocks (48–146 ppm, Wang et al., 2021) may not be due simply to variations in partition coefficients and magma compositions. On the micro-scale, Sc can be hosted as solid solutions in more than 100 minerals, and the intra-grain distribution of Sc is commonly highly heterogeneous and complex (McCarron et al., 2014; Čopjaková et al., 2015; Ubide et al., 2015; Cook et al., 2016). Deciphering the factors and processes behind the core-rim variations of Sc in clinopyroxene is essential to understanding the enrichment of Sc in minerals and the genesis of world-class Sc deposits.

In this study, we describe the occurrence of Sc in the Mouding deposit located in SW China, which is currently the largest known clinopyroxenite-hosted Sc deposit in the country. We illustrate the complex intracrystalline distribution of Sc in clinopyroxene by detailed studies of in-situ Sr isotopes, trace element concentrations, and electron backscatter diffraction (EBSD) analyses. The nucleation and growth history of clinopyroxene are examined by crystal size distribution (CSD) analysis in order to decipher the conditions favorable for formation of Sc-rich clinopyroxene. Our study shows that kinetic effects may play an important role in Sc partitioning in minerals.

2. GEOLOGICAL BACKGROUND OF THE MOUDING SC DEPOSIT

The South China Craton is composed of the Yangtze Block in the North and the Cathaysia Block in the South (Fig. 1A). The Yangtze Block has an Archean-Paleoproterozoic crystalline basement, which is unconformably overlain by Neoproterozoic and Sinian sedimentary successions (Zhao and Cawood, 2012). In the Yangtze Block, minor Archean and Paleoproterozoic basement assemblages are locally exposed in the northern part, whereas late Mesoproterozoic to early Neoproterozoic, metamorphosed, volcanic-sedimentary strata are widespread in the southeastern part (i.e., in the Jiangnan Orogen) and in the western and northern margins of the block (i.e., Panxi-Hannan Belt). Phanerozoic sedimentary rocks of the Yangtze Block are composed of interstratified limestone, dolomite, sandstone, conglomerate, black shale, and siliceous slate (Wang et al., 2013).

Widespread Permian continental flood basalts and related mafic–ultramafic intrusions of the Emeishan Large Igneous Province (ELIP) are exposed in the western part of the Yangtze Block (e.g., Zhang et al., 2006, 2009). The Mouding mafic–ultramafic intrusion is located in the SW part of the ELIP where it is bounded by the NS-trending Panzhihua and Lvzhijiang faults (Fig. 1A). Numerous mafic-(ultramafic) intrusions have been discovered around the periphery of the Mouding intrusion, such as the Aoxihe, Anyi, and Fulongji bodies (Fig. 1A), many of which are closely associated with magmatic Cu-Ni sulfide and Pt-group element (PGE) deposits. However, the ages of these intrusions are poorly constrained except for the Anyi (247 ± 3 Ma; Yu et al., 2014) and Zhubu (263 ± 6 Ma) bodies (Zhou et al., 2013; Tang et al., 2017). A few Mesoproterozoic granitic plutons are also exposed north of the Mouding intrusion (Fig. 1A; Fu et al., 2015).

The Mouding intrusion is likely coeval with the ELIP. It forms a horn-shaped lopolith dipping 30–20° to the southeast, which was formerly eroded and is now partially covered by Quaternary sediments. It has an exposed area of 0.15 km^2 with a core of monzogabbro that grades outward through syenogabbro, gabbro, and magnetite clinopyroxenite to clinopyroxenite (Fig. 1B and C). Several diorite dikes intrude the north and northeastern parts of the intrusion. The Sc-bearing ore bodies are mainly clinopyroxenites with an estimated Sc reserve of ~470 t at grades of 40–70 ppm Sc (Zhu, 2010). These bodies are generally massive and medium-grained with granular textures (Fig. 2), and consist of olivine (~5%), clinopyroxene (60–75%), Fe-Ti oxides (2–15%), K-feldspar (5–25%) and minor biotite (3–5%); the magnetite clinopyroxenites have similar mineral assemblages except for higher Fe-Ti oxides (15–25%) and generally lower K-feldspar (<10%). Most of the clinopyroxene grains are large (up to 8 mm long), euhedral, columnar crystals with clear boundaries. Primocrysts of clinopyrox-

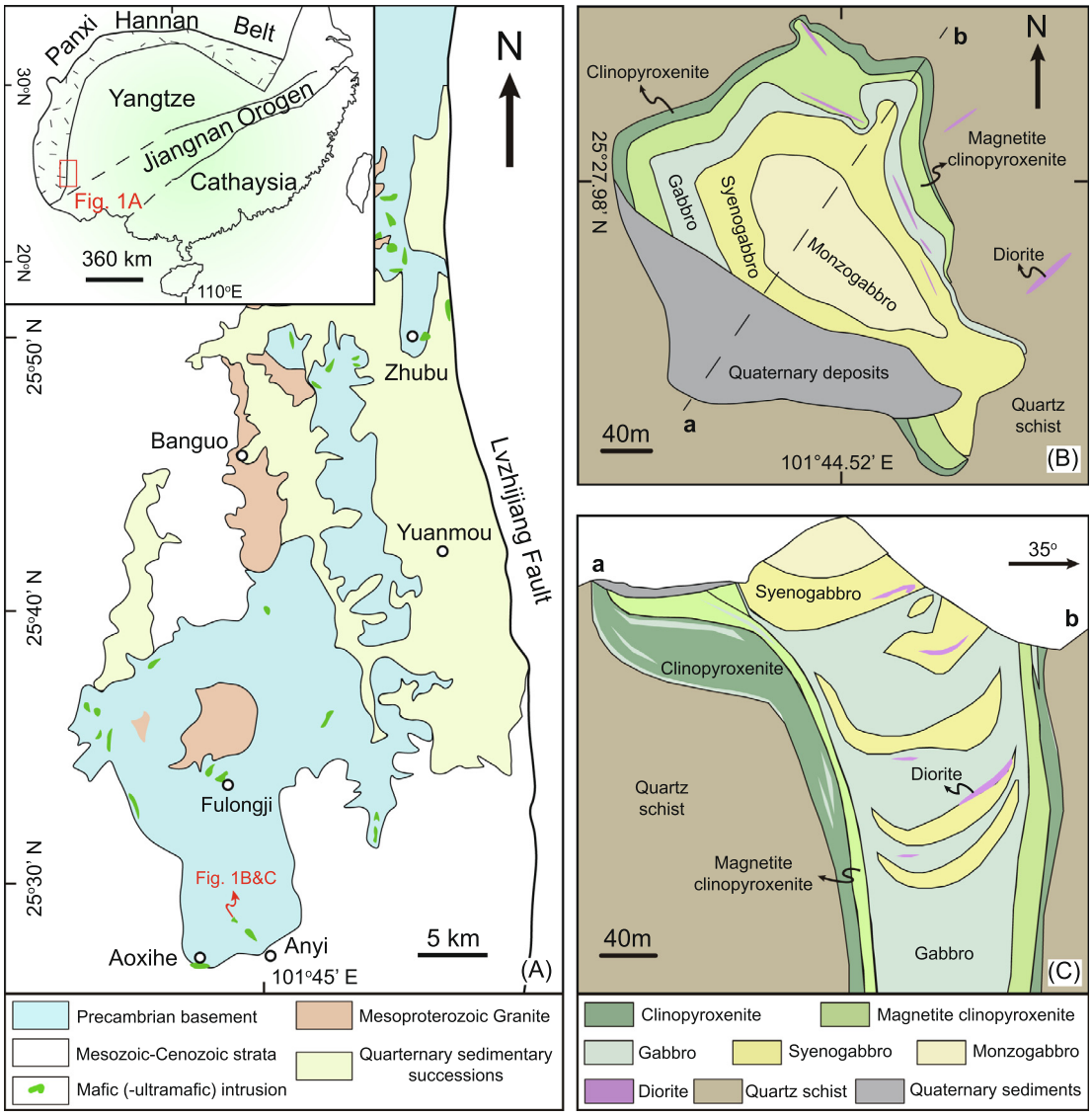

Fig. 1. (A) Distribution of mafic–ultramafic intrusions in SW China. The insert map shows the location of the study area. (B) A simplified geological map of the Mouding mafic–ultramafic intrusion. (C) Cross-section view of the intrusion (Guo et al., 2012).

ene form the framework of the rocks, and the interstices are filled with K-feldspar, magnetite, and minor biotite. Magnetite generally forms large, anhedral in grains the clinopyroxenite but small, euhedral crystals in the magnetite clinopyroxenite. Accessory minerals include apatite, pyrite and chalcopyrite, which are commonly enclosed in biotite and clinopyroxene.

3. METHODOLOGY

3.1. In-situ major element analysis

Major element compositions of the clinopyroxene were obtained with a JXA-8230 electron microprobe at The University of Hong Kong. The operating conditions were set at an accelerating voltage of 15 kV, a beam current of 20 nA, and a beam diameter of 2–4 μm. Peak counting times ranged from 10 to 30 s for different elements, and the background duration was 20 s. Data reduction followed ZAF correction procedures. The precisions for measured elements are better than 1%.

3.2. In-situ trace element analysis and mapping

Trace element compositions and whole-grain maps of the clinopyroxene were obtained by Laser Ablation Inductively Coupled Plasma Mass Spectrometry (LA-ICP-MS) on thin sections using a GeoasPro 193 nm ArF excimer laser coupled to a quadrupole-based Agilent 7900 MS at the Ore Deposit and Exploration Centre (ODEC), School of Resources and Environmental Engineering, Hefei University of Technology, Hefei, China. Analytical parameters were set at an ablation frequency of 10 Hz with an energy of 5 J/cm^2, and a spot diameter of 60 μm. Each anal-

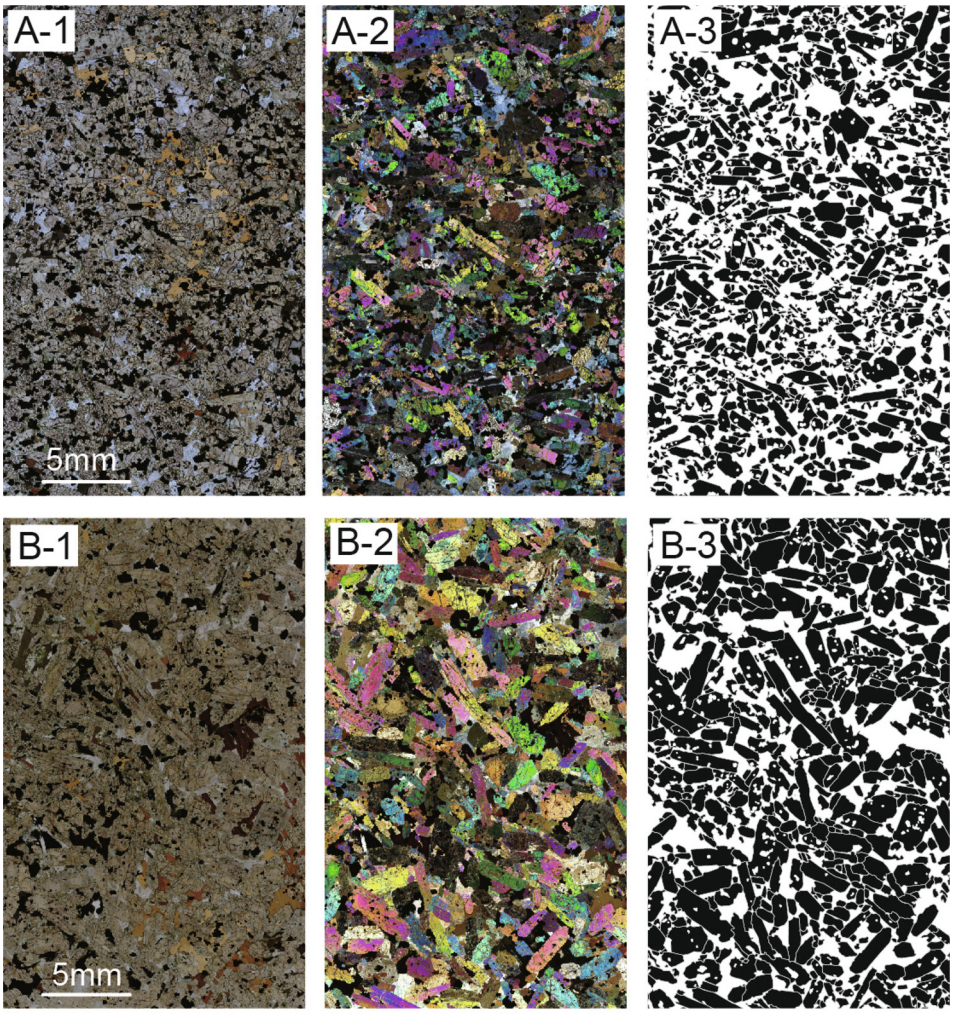

Fig. 2. Optical features and clinopyroxene distribution of (A) magnetite clinopyroxenite and (B) clinopyroxenite. A-1 and B-1 are photomicrographs under plane polarized light. A-2 and B-2 are photomicrographs under crossed polar. A-3 and B-3 are manually outlined clinopyroxene grains.

ysis consisted of 20 s background measurement, 40 s data acquisition, and 20 s Argon purification. Isotope ^{43}Ca was used as an internal standard, and multiple reference materials, including NIST 610, NIST 612, BIR-1G and BHVO-2G, were used as external standards for quantifying the trace element data. The standards were measured after every fifteen spot analyses. Time-drift corrections and data calibration were performed by ICPMSDataCal (Liu et al., 2008) and the precisions are better than 10%.

For element mapping, the laser beam was set at 30 μm with a speed of 20 μm/s. Images were compiled and processed using the empirical cumulative density function based on the LIMS (Laboratory Information Management System) (Wang et al., 2017), a user-friendly software based on Matlab that has similar functions to those of Monocle software (Petrus et al., 2017). The multiple external without internal standards calibration method was applied to overcome the matrix effects. Euhedral clinopyroxene crystal sections with clear and complete crystal faces free of visible inclusions were selected for mapping. Crystal section lengths ranged from 1.4 to 7.8 mm to assure a high resolution of the element mapping.

3.3. In-situ Sr isotope analysis

In-situ clinopyroxene Sr isotope compositions were obtained using a Neptune Plus Multi-Collector Inductively Coupled Plasma Mass Spectrometer (MC-ICP-MS) in combination with a Geolas HD excimer ArF laser ablation system at the Wuhan Sample Solution Analytical Technology Co., Ltd, Wuhan, Hubei, China. Spot sizes ranged from 90 to 160 μm depending on the Sr concentration of the clinopyroxene grain. The laser pulse energy was kept at ~10 J/cm^2 and the repetition frequency ranged from 8 to 15 Hz. The output data from the MC-ICP-MS were processed using Iso-Compass software (Zhang et al., 2020). A synthesized clinopyroxene glass (CPX05G, Sr = 518 ppm) was used to monitor the accuracy of the cal-

ibration method. A natural clinopyroxene megacryst (HNB-12) with a low Sr concentration (62.2 ppm) was analyzed as an internal standard and the measured results are consistent with the recommended isotope ratios ($^{87}Sr/^{86}Sr = 0.7040 \pm 0.0003$; Tong et al., 2016).

3.4. Crystal Size Distribution (CSD) analysis

The clinopyroxene CSD data were obtained by converting 2-D thin section measurements to 3-D textural parameters according to stereology theory (Higgins, 2000). Representative whole thin sections were scanned under a High-Resolution Olympus DSX1000 digital microscope. The grain boundaries were carefully outlined manually with the aid of cross-polarized light images, and any enclosed Fe-Ti oxides were excluded. More than 800 crystals were outlined in each thin section to reduce statistical uncertainties. The minimum crystal size outlined was ~0.01 mm. Incomplete crystals were excluded by an irregular envelope drawn around the outer rim of the thin section to avoid an edge effect. The 2-D apparent sizes and orientations of the crystals were measured by ImageJ (Schneider et al., 2012), and 3-D true crystal shapes were calculated by CSD slices (Morgan and Jerram, 2006). The best-fit short:intermediate:large (S:I:L) ratio of the crystal size (1:1.8:2.7, $R^2 = 0.9$) and an average crystal roundness of 0.6 was set to calculate the CSD patterns by CSDCorrection 1.6 (Higgins, 2000). In this study, the patterns are displayed in the form of typical semi-logarithmic diagrams (Marsh, 1988).

3.5. Electron Backscatter Diffraction (EBSD) analysis

Local crystal orientations of diopside were measured by EBSD with a Leo 1530 Field Emission Gun Scanning Electron Microscope at the Electron Microscope Unit, the University of Hong Kong. Thin sections were polished with a 0.05 μm alumina suspension for 8 hours, coated with a thin carbon layer, and tilted to 70° in the sample chamber. The accelerating voltage was set at 20 kV and the mapping was performed with a step size of 10 × 10 μm. Data acquisition and processing were achieved using the CHANNEL 5 software designed by HKL Technology APS Ltd. (Oxford, United Kingdom).

4. RESULTS

Diopside crystals from the clinopyroxenite units of the Mouding intrusion have high MgO (14.0–15.6 wt.%), CaO (21.4–22.5 wt.%) and TiO_2 (1.16–1.97 wt.%), but low Al_2O_3 (2.20–3.88 wt.%) and FeO (6.33–7.83 wt.%) contents (Table 1). They contain high Sc (80–105 ppm), V (230–346 ppm), Ni (132–179 ppm), and Sr (126–173 ppm), but have low total REE contents (71–110 ppm) (Table 2). The $^{87}Sr/^{86}Sr$ ratios of the clinopyroxene range from 0.7069 to 0.7084 (Table 2).

Various zoning patterns are visible under cross-polarized light (Fig. 2). Elongate clinopyroxene grains commonly show sector or hourglass zoning, whereas stout grains generally display banded zoning or are homogeneous. Four types of internal patterns of Sc distribution have been recognized. Representative euhedral diopside grains for each type are listed in Fig. 3 with more examples shown in Fig. S1. In the Type 1 distribution pattern, Sc is relatively homogeneous, except for some cracks showing low Sc contents. In the Type 2 pattern, Sc is enriched along the diopside rims, although the enrichment is commonly not symmetrical. Diopside grains showing Type 1 and 2 patterns are cut nearly perpendicular to the {0 0 1} faces, and their length to width ratios are both small (1.8–2.6). Type 3 distribution patterns of Sc are swallow-tailed, which is commonly semi-symmetrical, whereas Type 4 patterns are hourglass-shaped, and the enrichment areas are symmetrical. Diopside grains with Type 3 and 4 patterns are cut nearly perpendicular to the {1 0 0} or {0 1 0} faces, and their length to width ratios are high (3.0–4.0). Except for the Type 1 distribution pattern, the spatial distribution of Sc can be divided into Sc-rich and Sc-poor domains. Other trace elements in diopside, including Nb, Ta, Zr, Hf, REEs and V, as well as some major elements, such as Al and Ti, show broadly similar enrichment patterns with Sc (see Fig. 4 for representative grains and Fig. S2 for more examples).

5. DISCUSSION

Elemental zoning patterns in clinopyroxene, especially Type 2, are generally attributed to compositional variations of the host magma (e.g., Tecchiato et al., 2018; Li et al., 2020). If so, the Sc-rich domains would have resulted from either an increase of Sc content in the magma or an increase in the Sc partition coefficient between clinopyroxene and the melt ($D_{cpx\text{-}Sc}$). In order to test this hypothesis, we used in-situ element and Sr-isotope data of representative clinopyroxene grains. Results from the in-situ analyses are consistent with the compositional maps of Sc-rich and Sc-poor domains (Fig. 5B and C). Given that Sc is compatible in clinopyroxene, an evolved magma depleted in Sc would be expected to produce a Sc-poor domain on the rims of the diopside, which is not the case here. Alternatively, the enrichment of Sc along the rims could indicate replenishment by a more primitive magma with a higher Sc content. However, such a process should simultaneously lead to enrichment of Mg# values and Ni contents in the magma and consequently in the diopside that crystallized from it. This is inconsistent with the decrease of the Mg# values in the Sc-rich domains, and the overall constant Ni concentrations (Fig. 5D and E). Therefore, it is unlikely that the observed enrichment of Sc in Mouding diopside was due to an increase of Sc content in the magma.

Partition coefficients (D) of trace elements between clinopyroxene and melt vary with temperature, pressure, H_2O content, and melt composition. For Sc, the $D_{cpx\text{-}Sc}$ value is mainly controlled by the magma composition, in which the $LnD_{cpx\text{-}Sc}$ value has an excellent negative correlation with the LnMgO value ($R^2 = \sim 0.9$) (Bédard, 2014). Consequently, the observed decrease of the Mg# values in the Sc-rich domains (Fig. 5E) may correspond to an increase in $LnD_{cpx\text{-}Sc}$. Abrupt decreases in the MgO content of magma can result from the assimilation of silicious

Table 1
Major oxide compositions of clinopyroxene in clinopyroxenite and magnetite clinopyroxenite of the Mouding mafic–ultramafic intrusion.

Sample number	zk001-35-cpx-01	zk001-35-cpx-02	zk001-35-cpx-03	zk001-33-cpx-02	zk001-33-cpx-05	AY18-05-0001	AY18-5-0002	AY18-5-edge-5-01	AY18-5-edge-6-01	AY18-5-core-1-01	AY18-5-core-1-02	AY18-04 CPX-01	AY18-04 CPX-02	AY18-04 CPX-03	AY18-04 CPX-2-01	AY18-04 CPX-2-02
SiO_2	51.80	51.65	49.70	50.71	50.31	50.40	51.42	49.28	48.80	50.76	50.74	49.59	50.28	51.03	48.91	49.91
TiO_2	1.20	1.24	1.16	1.48	1.48	1.49	1.41	1.75	1.97	1.35	1.41	1.64	1.43	1.24	1.95	1.53
Al_2O_3	2.55	2.54	2.53	3.01	2.99	2.95	2.92	3.52	3.84	2.66	2.75	3.65	3.08	2.21	3.88	3.05
FeO	6.35	6.55	6.33	6.99	6.70	7.35	7.19	7.49	7.81	7.80	7.83	7.56	7.04	7.03	7.56	7.03
MnO	0.16	0.12	0.10	0.09	0.08	0.14	0.16	0.12	0.09	0.17	0.16	0.11	0.10	0.11	0.14	0.14
MgO	15.58	15.58	14.83	15.05	14.73	15.00	15.15	14.44	14.17	14.14	14.29	14.03	14.70	15.48	14.31	14.85
CaO	22.09	22.03	21.44	22.12	21.64	21.76	22.16	21.94	21.96	21.91	22.18	22.46	22.53	22.31	22.37	21.99
Na_2O	0.46	0.38	0.40	0.45	0.45	0.42	0.42	0.47	0.48	0.44	0.45	0.44	0.48	0.37	0.47	0.41
Total	100.19	100.09	96.49	99.90	98.38	99.51	100.83	99.01	99.12	99.23	99.81	99.48	99.64	99.78	99.59	98.91
Atom Units																
Si	1.902	1.900	1.897	1.873	1.887	1.871	1.883	1.841	1.824	1.898	1.885	1.847	1.863	1.886	1.818	1.863
Ti	0.033	0.034	0.033	0.041	0.042	0.042	0.039	0.049	0.055	0.038	0.039	0.046	0.040	0.034	0.055	0.043
Al(T)	0.098	0.100	0.103	0.127	0.113	0.129	0.117	0.155	0.169	0.102	0.115	0.153	0.135	0.096	0.170	0.134
Al(M1)	0.012	0.010	0.011	0.004	0.019	0.000	0.009	0.000	0.000	0.015	0.006	0.008	0.000	0.000	0.000	0.000
Fe^{3+}	0.052	0.048	0.055	0.073	0.043	0.076	0.060	0.098	0.106	0.043	0.063	0.085	0.094	0.090	0.119	0.084
Fe^{2+}	0.143	0.154	0.147	0.143	0.168	0.152	0.161	0.136	0.138	0.201	0.180	0.151	0.124	0.128	0.117	0.136
Mn	0.005	0.004	0.003	0.003	0.003	0.004	0.005	0.004	0.003	0.005	0.005	0.003	0.003	0.003	0.004	0.004
Mg	0.853	0.855	0.844	0.829	0.824	0.830	0.827	0.804	0.790	0.788	0.791	0.779	0.812	0.853	0.793	0.826
Ca	0.869	0.868	0.877	0.875	0.870	0.866	0.870	0.878	0.880	0.878	0.883	0.896	0.895	0.883	0.891	0.880
Na	0.033	0.027	0.030	0.032	0.033	0.030	0.030	0.034	0.035	0.032	0.032	0.032	0.034	0.027	0.034	0.030
Total	4.000	4.000	4.000	4.000	4.000	4.000	4.000	4.000	4.000	4.000	4.000	4.000	4.000	4.000	4.000	4.000
Mg#	81.4	80.9	80.7	79.3	79.7	78.4	79	77.5	76.4	76.4	76.5	76.8	78.8	79.7	77.1	79
Wo	45.3	45.1	45.6	45.6	45.7	45	45.4	45.8	46	46	46	46.9	46.5	45.2	46.4	45.7
En	44.5	44.4	43.9	43.2	43.3	43.1	43.1	42	41.3	41.3	41.3	40.8	42.2	43.7	41.3	42.9
Fs	10.2	10.5	10.5	11.2	11	11.9	11.5	12.2	12.8	12.8	12.7	12.3	11.3	11.1	12.3	11.4

Table 2
Major oxide, trace element and Sr isotopes of a representative diopside crystal. Analytical positions are shown in Fig. 5 (A) as blue dots.

Point	1	2	3	4	5	6	7	8	9	10	11	12	13	14	15	16	17	18	19	20	21	22
	Sc-poor domain															Sc-rich domain						
wt.%																						
SiO_2	52.1	51.9	51.9	52.0	51.7	51.6	51.6	51.7	51.4	51.4	51.4	51.2	51.3	51.3	51.3	48.6	48.9	48.6	49.0	49.2	49.2	49.7
TiO_2	1.12	1.10	1.09	1.11	1.15	1.08	1.08	1.09	1.11	1.10	1.09	1.17	1.11	1.11	1.10	1.66	1.60	1.70	1.54	1.47	1.47	1.40
Al_2O_3	2.22	2.20	2.20	2.21	2.26	2.34	2.30	2.28	2.29	2.30	2.24	2.45	2.24	2.24	2.23	4.16	4.15	4.25	3.84	3.46	3.54	3.55
FeO	6.01	6.05	6.04	6.09	6.13	6.07	6.04	6.01	6.02	6.09	6.08	6.14	6.00	6.13	6.00	6.67	6.55	6.62	6.43	6.38	6.43	6.04
MnO	0.17	0.17	0.17	0.17	0.16	0.17	0.17	0.17	0.17	0.17	0.17	0.17	0.17	0.17	0.17	0.16	0.16	0.16	0.16	0.16	0.16	0.17
MgO	16.1	16.1	16.2	16.2	16.2	16.1	16.3	16.2	16.3	16.3	16.4	16.4	16.4	16.5	16.5	15.5	15.6	15.6	15.8	16.1	16.2	15.8
CaO	21.7	21.9	21.8	21.6	21.9	22.0	21.9	22.0	22.1	22.0	22.0	21.9	22.1	22.0	22.1	22.5	22.4	22.4	22.5	22.5	22.3	22.7
Na_2O	0.28	0.28	0.29	0.28	0.29	0.30	0.31	0.29	0.30	0.30	0.30	0.32	0.35	0.30	0.29	0.35	0.36	0.35	0.35	0.35	0.35	0.37
ppm																						
Li	5.01	4.53	4.05	4.66	4.68	3.76	3.58	4.08	3.59	4.01	4.38	4.19	3.16	4.02	4.68	4.26	3.71	4.58	3.89	3.53	4.22	3.47
Sc	86.2	84.8	82.4	84.2	85.3	80.0	82.4	82.2	84.2	82.0	82.0	84.2	83.4	83.0	83.6	105	104	97.1	99.4	91.7	92.3	81.9
V	236	235	230	236	240	239	235	238	239	240	239	245	239	236	236	346	339	335	323	302	306	279
Cr	25.3	23.5	24.1	23.9	24.6	25.4	26.2	25.3	24.1	26.1	25.5	27.4	24.7	25.0	25.5	39.5	39.6	38.2	38.7	36.6	35.0	13.8
Co	57.8	57.7	56.9	57.6	57.2	56.5	55.6	57.1	57.1	56.8	56.8	57.7	56.1	59.7	57.1	57.6	56.7	56.1	56.2	57.1	57.5	50.7
Ni	174	174	171	172	174	173	175	179	173	173	174	173	171	178	176	169	176	176	176	173	175	132
Cu	0.40	0.44	0.51	0.08	0.24	0.00	0.16	0.04	0.00	0.33	0.24	0.21	0.29	0.00	0.08	0.03	0.34	0.30	0.10	1.92	0.00	0.26
Zn	35.9	36.8	39.0	39.3	39.0	35.3	38.6	39.0	38.8	36.8	37.4	39.0	37.3	39.8	39.1	36.3	35.9	36.3	41.0	36.9	37.6	34.4
Ga	5.77	5.57	5.45	5.65	5.91	6.32	5.83	5.82	5.61	6.06	6.18	6.41	6.63	5.83	6.02	9.38	9.25	10.2	8.87	8.48	8.11	8.57
Ge	3.48	2.84	2.03	4.23	2.16	2.93	2.39	3.79	2.85	4.40	3.26	4.20	3.85	2.34	3.55	2.76	3.76	3.46	2.93	3.94	4.20	3.69
As	1.18	1.08	0.19	0.72	0.00	1.62	0.28	0.63	1.08	0.15	0.00	0.12	1.15	1.06	0.77	1.01	0.92	0.05	1.40	1.28	0.64	0.85
Sr	131	132	130	129	136	126	133	132	130	129	128	135	144	132	133	157	159	156	159	149	148	173
Y	9.50	9.55	9.33	9.60	9.59	9.88	9.79	9.23	9.65	9.22	9.33	9.86	10.2	9.33	9.54	13.0	12.2	12.6	11.7	11.0	11.2	13.0
Zr	44.4	41.0	40.4	42.5	44.9	44.7	39.5	41.6	43.8	39.5	41.5	46.9	46.8	42.7	43.3	82.8	82.2	79.8	72.6	62.3	65.7	73.0
Nb	0.16	0.16	0.17	0.12	0.28	0.21	0.26	0.22	0.24	0.16	0.16	0.27	0.28	0.18	0.20	0.39	0.35	0.54	0.48	0.43	0.40	0.35
Sn	1.28	1.35	1.12	1.70	1.96	1.25	1.37	1.37	1.40	1.58	1.19	1.73	1.58	1.80	1.31	2.38	1.87	1.96	2.16	1.50	1.55	1.69
Ba	0.10	0.16	0.10	0.11	0.00	0.16	0.06	0.21	0.13	0.16	0.21	0.13	0.13	0.13	0.06	0.06	0.00	0.08	0.07	0.19	0.14	0.23
La	7.59	7.47	7.61	7.46	7.97	6.94	7.93	7.66	7.74	7.22	7.28	8.62	9.43	7.38	7.34	12.13	11.55	11.43	10.90	9.91	10.23	11.33
Ce	24.97	24.82	24.51	24.68	25.66	23.65	25.49	25.26	24.80	24.98	24.54	28.36	29.90	25.33	24.42	38.60	37.75	38.31	35.39	32.91	32.62	38.02
Pr	4.38	3.97	3.94	4.16	4.45	3.84	4.13	4.07	4.29	4.07	3.86	4.54	4.92	4.26	4.18	6.41	6.02	6.27	5.48	5.19	5.21	6.24
Nd	22.76	21.77	20.61	22.14	22.41	20.78	20.91	21.89	21.85	21.18	21.22	24.45	23.43	21.18	21.74	32.67	31.77	31.66	29.49	27.43	26.51	32.18
Sm	5.16	4.48	4.20	5.06	5.34	5.22	4.83	5.16	4.63	4.92	4.53	5.38	4.54	4.77	4.75	6.49	6.79	7.24	6.37	5.98	5.63	7.33
Eu	1.31	1.36	1.32	1.45	1.51	1.29	1.36	1.32	1.38	1.27	1.37	1.36	1.43	1.42	1.40	1.84	1.85	1.80	1.64	1.75	1.63	2.02
Gd	3.90	3.60	3.96	4.11	3.81	4.13	3.67	3.53	3.75	3.63	3.75	3.80	3.96	3.66	3.88	5.31	5.42	5.07	4.98	4.56	4.01	5.69
Tb	0.51	0.52	0.44	0.55	0.49	0.45	0.46	0.49	0.51	0.49	0.48	0.46	0.50	0.43	0.46	0.67	0.65	0.61	0.58	0.53	0.58	0.75
Dy	2.25	2.46	2.29	2.30	2.38	2.47	2.00	2.44	2.68	2.23	2.12	2.59	2.35	2.54	2.55	3.28	3.07	3.31	3.04	2.58	2.55	3.44
Ho	0.42	0.41	0.40	0.40	0.48	0.37	0.40	0.38	0.45	0.38	0.40	0.41	0.39	0.36	0.41	0.57	0.55	0.56	0.55	0.48	0.45	0.57
Er	0.98	0.97	0.81	0.93	0.81	0.89	0.86	1.03	0.87	0.90	1.00	0.88	0.82	1.13	0.83	1.25	1.31	1.31	1.08	0.94	1.08	1.31
Tm	0.11	0.09	0.10	0.12	0.13	0.11	0.11	0.09	0.11	0.10	0.09	0.10	0.09	0.10	0.12	0.15	0.15	0.17	0.13	0.14	0.12	0.19

Yb	0.81	0.72	0.74	0.81	0.59	0.66	0.86	0.68	0.67	0.61	0.80	0.84	0.95	0.46	0.59	0.88	0.65	0.83	0.74	0.81	0.96	0.91
Lu	0.08	0.09	0.13	0.11	0.11	0.07	0.07	0.10	0.08	0.10	0.07	0.10	0.11	0.07	0.11	0.13	0.12	0.12	0.13	0.13	0.16	0.16
Hf	1.98	2.07	2.01	2.19	2.24	2.10	1.93	2.20	2.18	2.06	2.14	2.39	2.39	2.22	2.03	4.23	3.88	4.04	3.85	3.07	3.23	3.55
Ta	0.05	0.04	0.02	0.02	0.04	0.03	0.03	0.02	0.03	0.02	0.02	0.04	0.04	0.01	0.03	0.08	0.07	0.07	0.09	0.06	0.06	0.07
Pb	0.15	0.14	0.14	0.12	0.12	0.18	0.11	0.13	0.11	0.15	0.14	0.15	0.12	0.15	0.10	0.14	0.17	0.18	0.14	0.09	0.11	0.13
Th	0.08	0.06	0.04	0.04	0.06	0.05	0.11	0.07	0.03	0.06	0.04	0.09	0.09	0.05	0.03	0.11	0.08	0.13	0.13	0.12	0.15	0.05
$^{87}Sr/^{86}Sr$	0.70721	0.70806	0.70793	0.70745	0.70755	0.70770			0.70750	0.70836		0.70838	0.70785	0.70812		0.70756	0.70775	0.70799	0.70692	0.70694	0.70703	0.70748
2SE	0.00048	0.00029	0.00031	0.00027	0.00026	0.00029			0.00043	0.00028		0.00036	0.00028	0.00034		0.00026	0.00023	0.00024	0.00025	0.00025	0.00029	0.00026

rocks, which is consistent with the elevation of Sr concentrations in the Sc-rich domains (Fig. 5F). However, such an interpretation is not supported by the constant $^{87}Sr/^{86}Sr$ values (Fig. 5G). Therefore, we conclude that compositional changes in the melt, coupled with variations in $D_{cpx\text{-}Sc}$, did not cause the observed Sc variations in the Mouding clinopyroxene, or at least they were not the primary controls.

Subsolidus re-equilibration during magma cooling may produce core-rim variations, which can be complicated by anisotropic diffusion (e.g., Cherniak and Liang, 2007; Sun, 2021). Unfortunately, a lack of diffusion rate for Sc in diopside precludes direct testing of this hypothesis. Nonetheless, Sc has similar distribution patterns with Al (Fig. 4), which has a low diffusion rate in clinopyroxene (Watson and Liang, 1995), implying that the diffusion rate of Sc should be low as well and the effect of subsolidus diffusive exchange of Sc should be negligible.

5.1. Kinetic control on Sc distribution in diopside

Previous studies of Ti-rich augite have shown that Al and Ti have a stronger tendency to be incorporated into the {1 0 0}, {1 1 0}, and {0 1 0} faces than in the {1 1 1} face when the degree of supercooling (ΔT) is lower than 32 °C (Masotta et al., 2020). Some trace elements also show preferential enrichment in the {1 0 0}, {1 1 0}, and {0 1 0} faces, such as Nb, Ta, Zr, Hf, REEs and V in the prism sectors, which are attributed to their high sensitivities to crystallization kinetics (Ubide et al., 2019). However, Sc does not appear to follow this rule, as evidenced by its enrichment in concentric zones (Ubide et al., 2019), leading to the conclusion that Sc distribution is mainly controlled by magma recharge or mixing. However, our study shows that Al, Ti, Nb, Ta, Zr, Hf, REEs, V, and Sc all have similar distribution patterns in our studied diopside crystals (Fig. 4), implying that they are controlled by similar processes. EBSD analysis indicates that Type 1 and 2 distribution patterns are perpendicular to the {0 0 1} face, whereas Type 3 and 4 patterns are perpendicular to the {0 1 0} or {1 0 0} faces (Fig. 3; Fig. S1). Given that prismatic Al and Ti cross-cutting patterns in Ti-rich augite (Welsch et al., 2016; Ubide et al., 2019) are similar to those of the Type 3 patterns of Sc in this study, we propose that the enrichment of Sc in clinopyroxene is also due to preferential incorporation at specific crystal faces.

If crystal growth is due to the gradual adsorption of layers of unit cells on each face, the development of sector or hourglass zoning would mainly be reflecting the characteristics of the adsorption layers (Dowty, 1976). The admissibility of cations into different adsorption layers depends chiefly on the configuration of protosites, which are partially formed structural sites on crystal surfaces (Nakamura, 1973). Protosites with higher flexibility would generally be more replaceable. The flexibility of protosites can be inferred by the least number of bonds divided by the total number of potential bonds in the first coordination sphere to the crystal side (Nakamura, 1973). Scandium has an ionic radius similar to that of Mg (Shannon, 1976), and prefers octahedral M1 sites in diopside with coordination

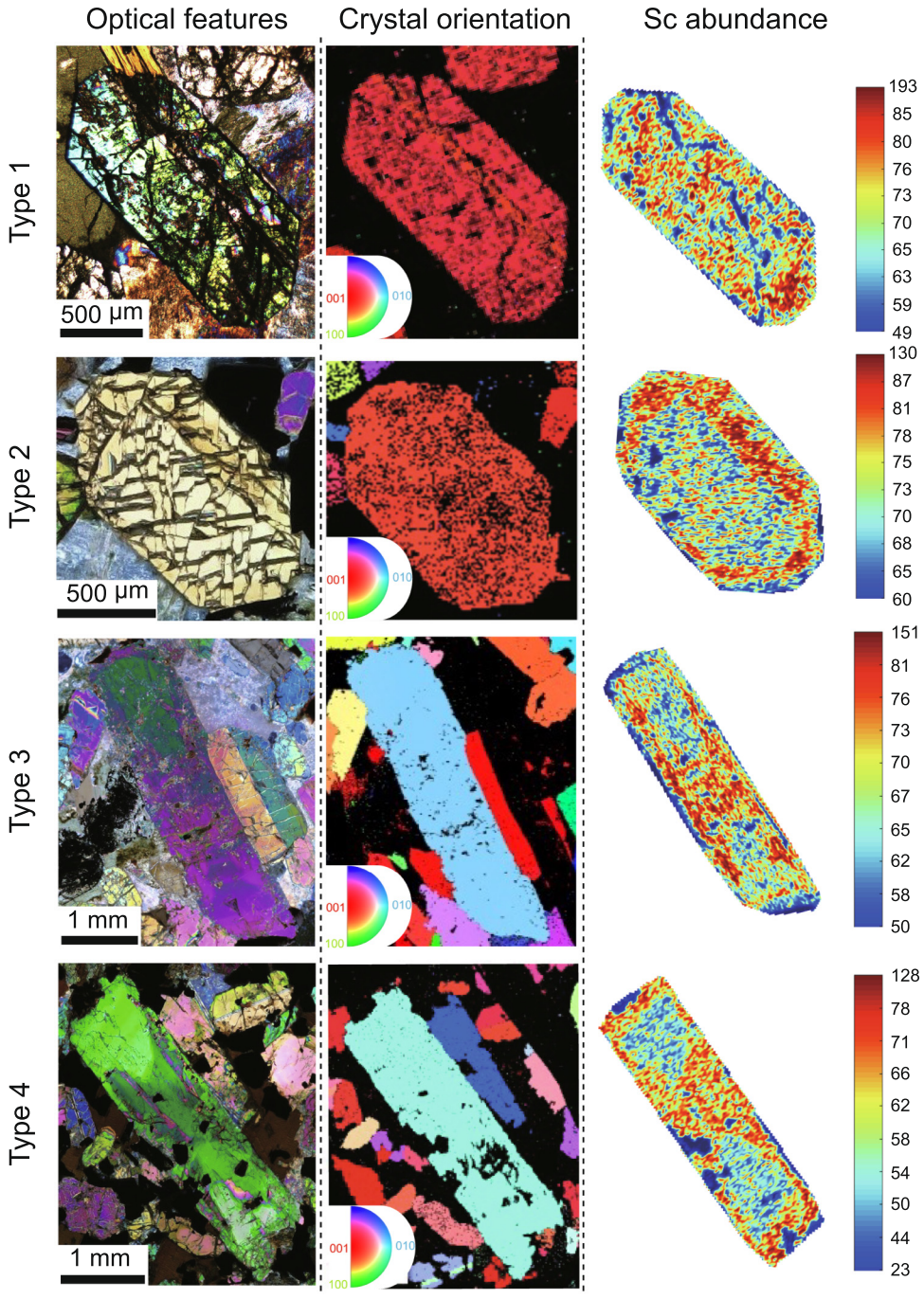

Fig. 3. Characteristics and Sc distribution patterns for diopside crystals in the Mouding intrusion. The first column (1–4) refers to the four Sr distribution patterns in our study. Column two shows photomicrographs under a petrographic microscope showing optical features of the grains under crossed polar. Column three show the crystal orientations from EBSD analysis. The colors (red, cyan, and green) indicate the {0 0 1}, {0 1 0}, and {1 0 0} orientations perpendicular to the plane of the page, respectively. Column four provides distribution maps of Sc abundance in each grain from the LA-ICP-MS trace element mapping. The color columns on the righthand side reflect the abundance of Sc in the grains with absolute values in ppm. More EBSD analytical results are shown in Fig. S1. (For interpretation of the references to colour in this figure legend, the reader is referred to the web version of this article.)

numbers of 6 (Nazzareni et al., 2013). For the M1 site, three types of protosite configuration are commonly shown: the 3/6, 4/6, and 5/6 sites (Fig. 6A1–A3). The 3/6 site is the most preferable configuration for substitution because it has the highest flexibility. Significant degrees of substitution can also occur at the 4/6 site, whereas the 5/6 site has a low preference for foreign cations (Dowty, 1976).

Modeling of the protosite configuration of diopside was performed with the aid of VESTA software (Momma and Izumi, 2011). Classical cell parameters for diopside were adopted (a = 9.946, b = 8.899, c = 5.251 Å, β = 105.63°)

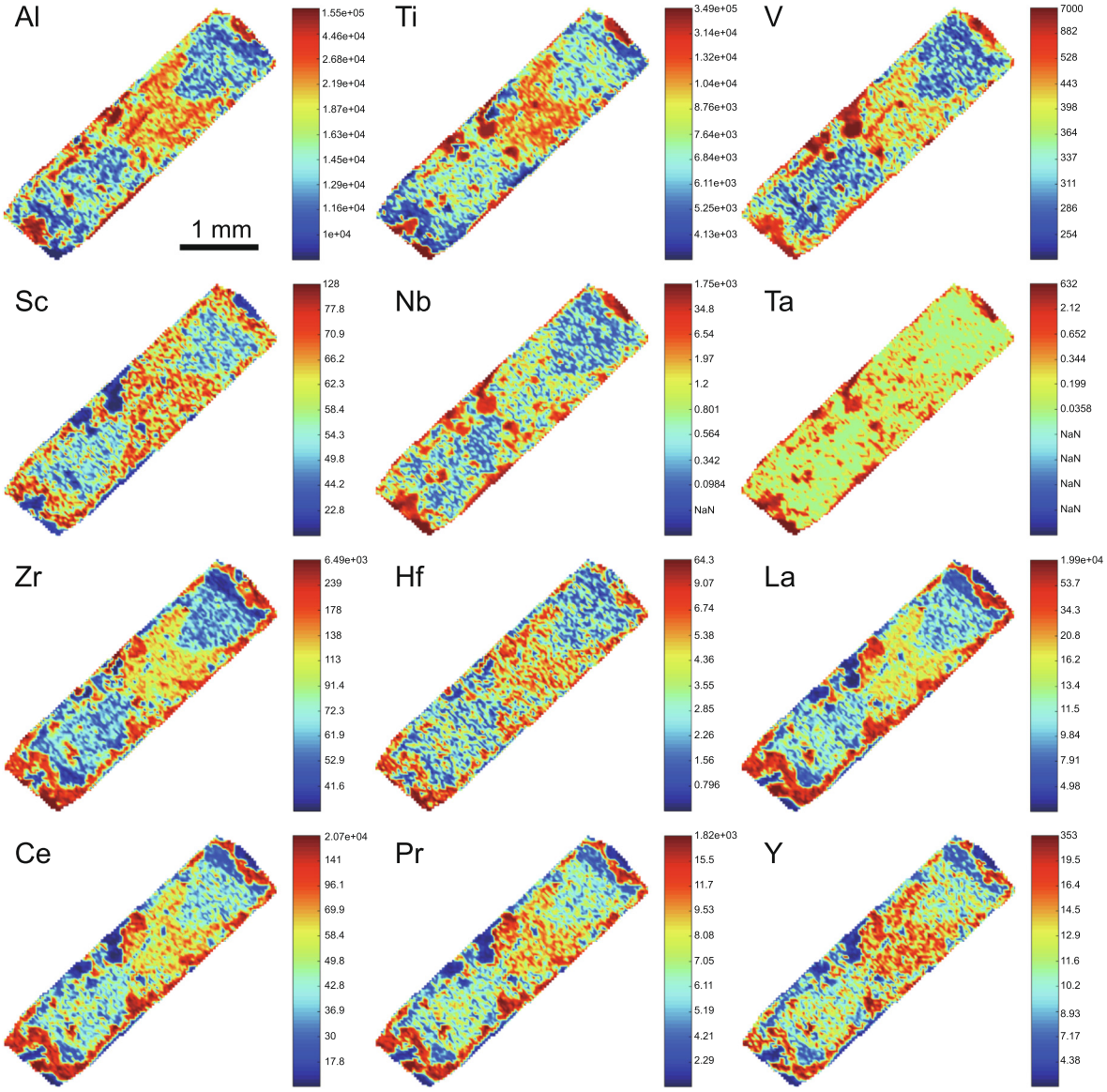

Fig. 4. Minor and trace element mapping of euhedral diopside grains showing similar enrichment patterns of Al, Ti, V, Nb, Ta, Zr, Hf, REEs and Sc. More examples are shown in Fig. S2.

with the space group C 1 2/c 1 (Clark et al., 1969). Atom positions were set as suggested by Cameron et al. (1973). The protosite configuration of each face was obtained by adjusting the cutoff faces and rotating the visual angle. The M1 site on the {1 0 0} face has a 3/6 configuration, implying that {1 0 0} should be the most favorable surface for Sc substitution (Fig. 6). A moderate amount of Sc can be adsorbed on the {0 1 0} and {1 1 0} faces as suggested by their 4/6 site configuration. However, Sc cannot easily enter protosites on the {0 0 1}, {1 1 1} or {2 2 –1} faces due to their 5/6 configurations. Uncommon {0 2 1}, {3 3 –1}, {3 1 0}, {3 1 3}, {–3 1 2}, and {5 0 1} faces may also form (Groth and Krantz, 1880), but the M1 sites of each of these display 5/6 configurations (Fig. 6). Therefore, Sc incorporation into diopside is most likely to occur at the {1 0 0}, {0 1 0}, and {1 1 0} faces.

To simulate the observed Sc distribution patterns, we modeled the growth of diopside grains in relation to the generation of different patterns (Fig. 7). Modeling of the crystal shape and zoning was performed using the software SHAPE 7.4 (Dowty 1980, 1987). The central distances of the {1 0 0}, {0 1 0} and {0 0 1} faces are 1.0, 1.8, and 2.7, respectively, following the S:I:L ratios that were obtained from CSD analyses in this study. The central distances for {1 1 0}, {1 1 1}, and {2 2 –1} were set arbitrarily at 1.6, 2.7, and 2.8, respectively, to best fit the apparent section geometry. Uncommon faces were not modelled to avoid confusion.

Sector zoning of diopside was reconstructed by assuming a linear growth rate for each face (Table 3). In this scenario, the Type 1 and 2 Sc distribution patterns can be simulated by a series of horizontal sections, i.e., parallel

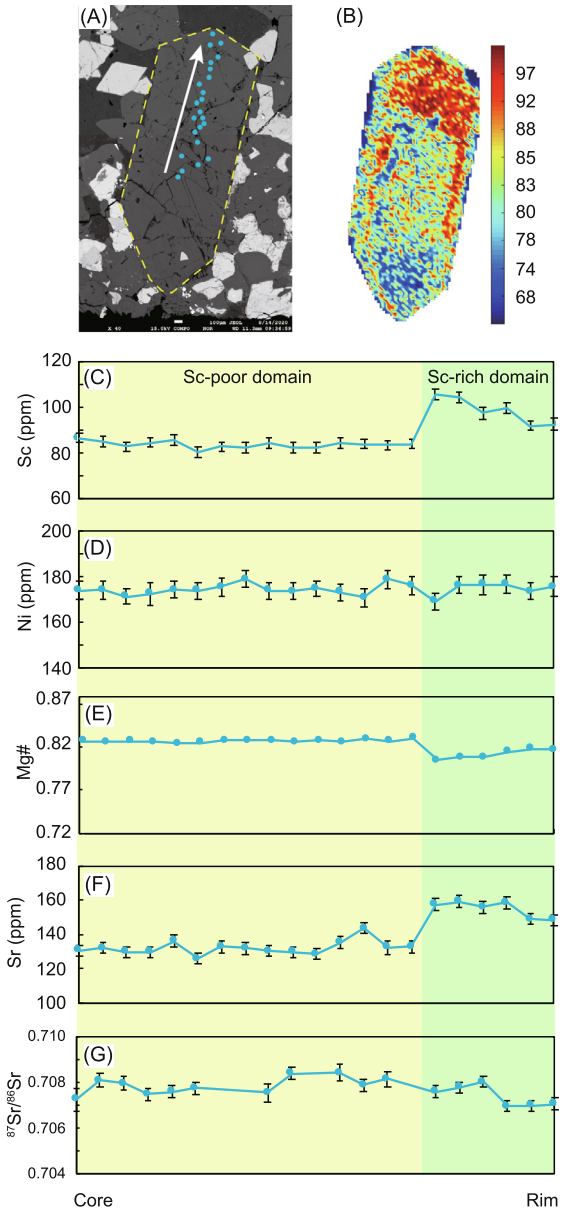

Fig. 5. *In-situ* major, trace element, and Sr isotope compositions of a representative diopside crystal from core to rim. Analytical positions are denoted by the blue dots in Fig. A. The results are given in Table 2. Figs. C–G record compositional trends along the line of analysis.

to the {0 0 1} face, at different central distances (Fig. 7AI-1 and AI-2). The Type 3 Sc pattern can be reproduced by vertical sections parallel to the {0 1 0} or {1 0 0} face at different central distances (Fig. 7AII-1 and AII-2). However, the Type 4 Sc distribution pattern cannot be reproduced for any section orientation, because the prismatic faces must always be depleted in Sc. Alternatively, assuming an exponential growth rate for the basal faces, and a linear growth rate for the prism faces (Table 3), the boundaries between the prismatic and basal faces would be curved rather than linear. Tilted sections can then intersect the prism–sector–prism faces and produce the Type 4 Sc distribution pattern (Fig. 7BII-3). Furthermore, the Type 1–3 Sc distribution patterns can still be produced in this scenario (Fig. 7BI-1, BI-2, BII-1 and BII-2). This simple simulation shows that the growth rates of the basal faces in diopside are not constant, but rather that the Sc distribution patterns are largely related to the growth rate of each face.

5.2. Magmatic growth of diopside and Sc enrichment

Quantitative analysis of rock textures can aid in understanding the dynamics and cooling history of magma bodies and help decipher the nucleation and coarsening processes of crystals (e.g., Marsh, 1988). The CSD of diopside in clinopyroxenite from the Mouding intrusion deviates from the ideal initial CSD pattern by being concave downward at small crystal sizes, which is reversed at the 2.5 mm size (Fig. 8A). The slopes and intercepts of the offset CSD patterns are obviously negatively correlated (Fig. 8B), indicating the absence of small grains during crystal coarsening. These observations are consistent with the communicating neighbor model of textural coarsening, which commonly occurs when the temperature is close to the liquidus so that mineral growth rates are high, whereas the nucleation rates are close to zero (Higgins, 1998). In natural systems, magmas deviate significantly from dilute liquids, hence the growth rates of crystals are influenced not only by their individual sizes but also by their distance to neighboring minerals (DeHoff, 1991). Studies on natural systems show that larger grains have higher growth rates than smaller grains, and that CSD patterns become flattened as crystals grow and coarsen (Higgins, 1998, 2002). The fast growth of large clinopyroxene crystals in the Mouding intrusions may have played an important role in promoting the kinetic controls on element partitioning.

Textural coarsening can maintain permeability in a magma body, even for high crystal abundances, because smaller crystals, which tend to hinder melt circulation, would be dissolved in this process. Another coarsening mechanism, adcumulus growth, is common in plutonic rocks, particularly in layered intrusions (e.g., Higgins, 2002). In this process, all crystals tend to grow equally, resulting in coarsening of small crystals and isolation of interstitial melts, which then causes a deficiency of compatible elements along the rims of the crystals (e.g., Gao et al., 2007). In this case, the influence of magma composition may surpass that of kinetic control on the enrichment of Sc in clinopyroxene. Clearly, textural coarsening is favored over adcumulus growth during the formation of Sc-rich clinopyroxene because active liquid flow and efficient interstitial communication can direct Sc from the entire magma chamber and from any replenished magma, into the clinopyroxene. Given that elements can be transferred from small grains into larger grains via diffusion (Higgins, 2002), the growth rate of crystals would largely be influenced by the diffusion rate of specific elements in the magma, which in turn, is controlled by the magma viscosity. We propose that low magma viscosities and, therefore, high volatile contents, profoundly influence textural coarsening. This is supported by the commonly identified textural coarsening in hydrous magmatic systems (e.g., natrocarbonatite;

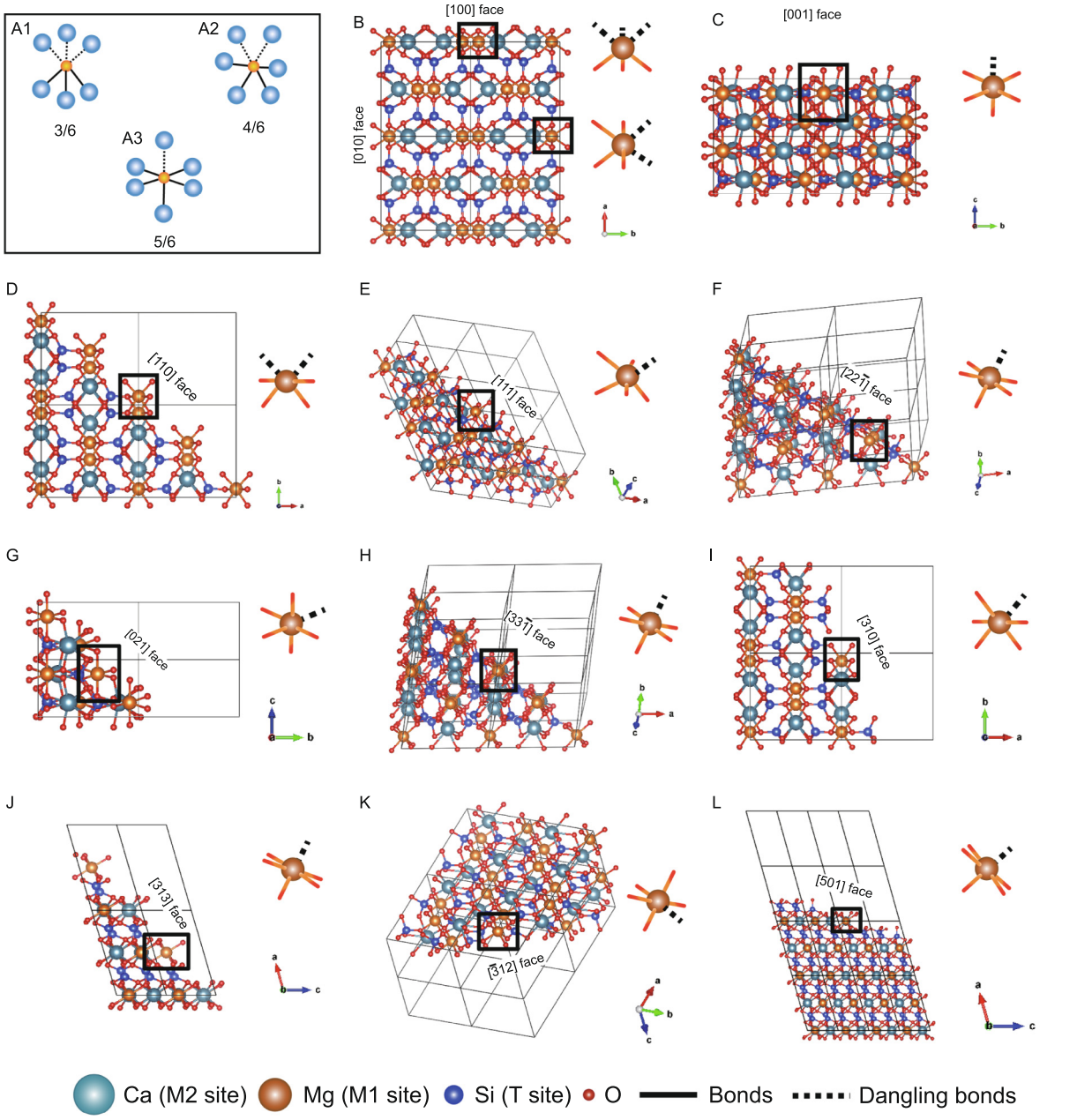

Fig. 6. (A) Typical protosite configuration of octahedral cation sites. (B–L) Octahedral protosite configuration on different exposed crystal faces of the diopside. The modeling technique is described in the main text.

Mattsson and Caricchi, 2009) or with volatile-rich minerals (e.g., amphibole in basalt and fluorapatite in mafic intrusions; Zhang et al., 2019; Wang and Wang, 2020).

5.3. Implications for Sc enrichment in minerals and disequilibrium crystallization

Deciphering the Sc incorporation mechanisms in minerals is critical to understanding the Sc enrichment processes and the genesis of Sc deposits. A variety of minerals in addition to clinopyroxene show variable degrees of Sc enrichment within individual crystals (e.g., Eby, 1973; Liferovich et al., 1998; Wise et al., 1998; Kempe and Wolf, 2006). Studies of Sc enrichment are sparse, and the reasons for intra-grain variations of Sc remain ambiguous. Our study shows that trace element mapping, coupled with local crystal orientation, is a feasible way to study this problem.

Except for simple core-rim variations, which presumably result from compositional variations of magmas (e.g., Ubide et al., 2015), the distribution patterns of Sc in individual grains, such as co-existing banded patterns subparallel to the crystal boundaries and patchy patterns in the centers of garnet grains (Cook et al., 2016), or dendritic patterns in the centers of epidote grains (Čopjaková et al.,

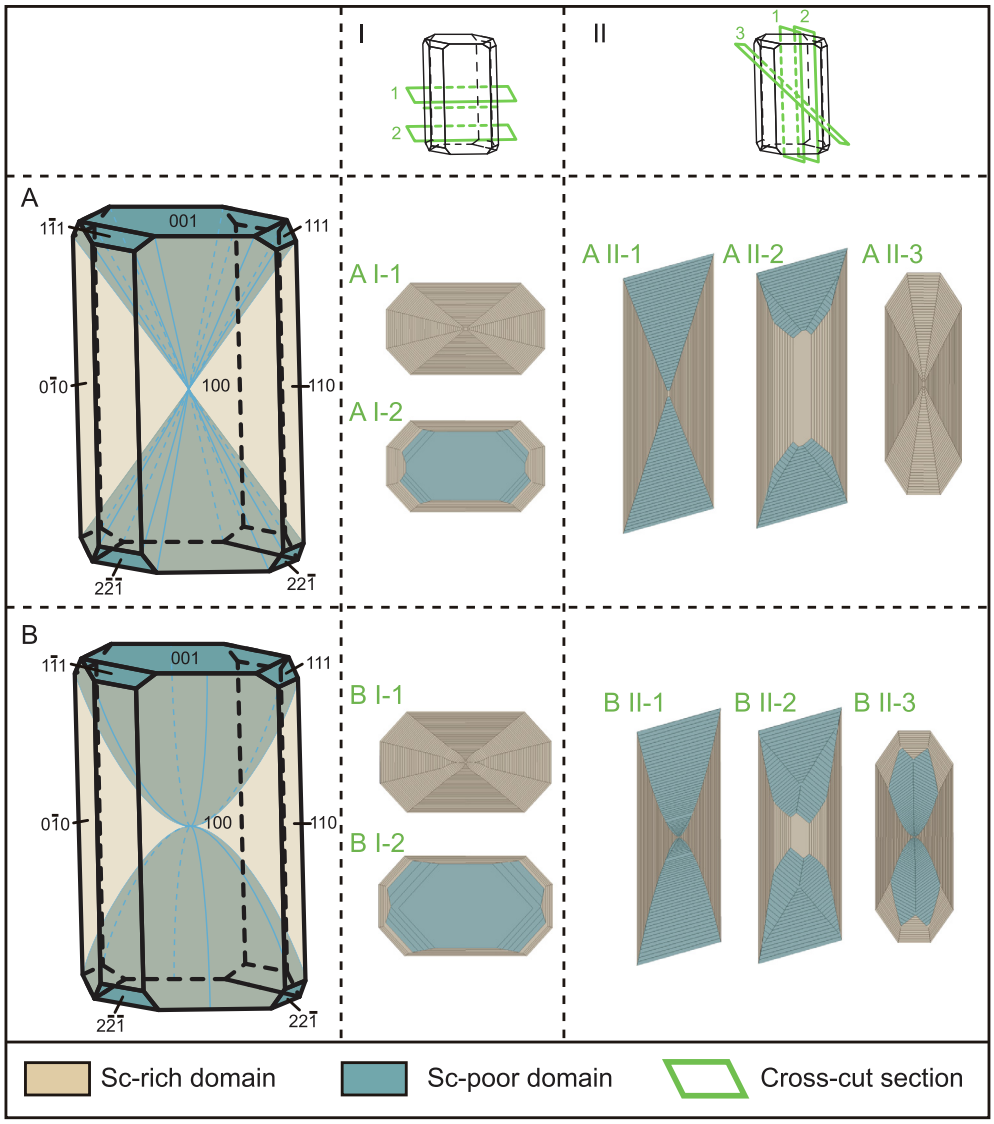

Fig. 7. The crystal shape and zoning of the diopside assuming (A) linear growth of all faces and (B) linear growth of prismatic faces and exponential growth of basal faces. The modeling technique is described in the text.

Table 3
Growth rates of different crystal faces needed to form sector zoning and hourglass zoning calculated using the SHAPE software. Time (T) ranges from 0 to 1. The increment is set as 0.02.

Crystal faces	Sector zoning	Hourglass zoning
{1 0 0}	1.00	1.00
{0 1 0}	1.80	1.80
{1 1 0}	1.60	1.60
{0 0 1}	2.70	0.75 + 1.17 T
{1 1 1}	2.70	0.75 + 1.17 T
{2 2 1}	2.80	0.75 + 1.27 T

2015), are difficult to explain. We note that minerals with complex Sc distribution patterns are commonly formed in fluid-rich systems, in which the growth rates of minerals are facilitated by the low viscosity and high ion diffusion rate, which favor textural coarsening (Higgins, 2002). Nano-scale kinetic effects on trace element zoning have been demonstrated during mineral crystallization (Wu et al., 2019) and pseudomorphic replacement reactions have been shown to occur in hydrous environments (Xia et al., 2009). Given that many Sc deposits are closely related to volatile-rich magmas, especially Alaskan-type mafic–ultramafic intrusions that are closely related to arc magmas, kinetic processes may also govern Sc enrichment of minerals in these bodies. We suggest that in addition to compositional variations of magmas, selective substitution of Sc by other trace elements, and changes in partition coefficients, kinetic effects may also be important for Sc enrichment in minerals.

The close association of Sc with HFSEs has long been recognized in many minerals (e.g., Gramaccioli et al., 2000; Williams-Jones and Vasyukova, 2018). This was

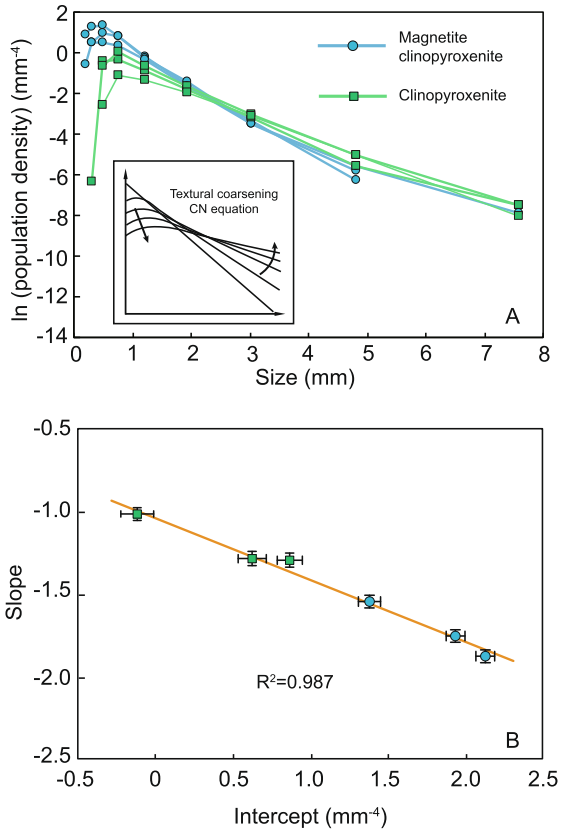

Fig. 8. (A) CSD of clinopyroxene in magnetite clinopyroxene and clinopyroxenite, with the communicating neighbor model modified from Higgins (2002). (B) Correlations between the slope and intercept of the offset CSD patterns.

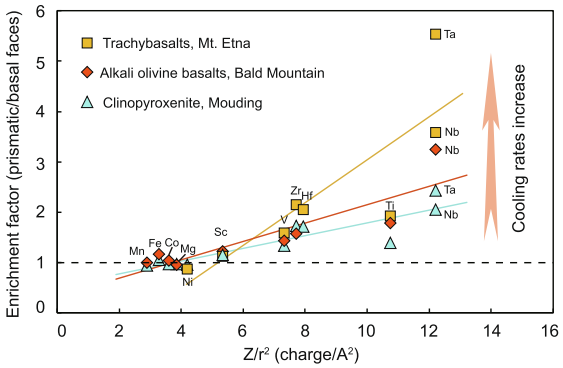

Fig. 9. Positive correlation between the element enrichment factor (prismatic face concentration versus basal face concentration) and their charge versus radii (cation radii from Shannon, 1976). Only elements that tend to be incorporated in the clinopyroxene octahedral M1 site are shown for clarity. Trachybasalts from Mt. Etna (Ubide et al., 2019) have fine to glassy groundmasses, implying faster cooling rates than those seen for the alkali olivine basalts from Bald Mountain (Shimizu, 1981), which have a holocrystalline groundmass and granular clinopyroxenite similar to that seen in the Mouding mafic–ultramafic intrusion. Faster cooling rates may have promoted disequilibrium crystallization and increased the enrichment factors of elements in the clinopyroxene.

explained by either coupled substitution of Sc and HFSEs, such as $Fe^{2+} + W^{6+} = Sc^{3+} + (Nb,Ta)^{5+}$ in wolframite (Kempe and Wolf, 2006) and $Sc^{3+} + (Ti,Sn)^{4+} = (Fe, Mn)^{2+} + (Nb,Ta)^{5+}$ in columbite (Wise et al., 1998) or the existence of HFSEs-bearing inclusions in Sc-rich minerals (Foord et al., 1993). Our study shows that kinetically controlled growth can also lead to positive correlations between Sc and HFSEs such as Nb, Ta, Zr, Hf, Ti and V (Fig. 9), because HFSEs and Sc all have high activation energies of desorption, which would likely cause them to concentrate on prismatic faces (Shimizu, 1981; Ubide et al., 2019).

Hourglass zoning of clinopyroxene has commonly been documented in volcanic rocks, especially alkaline basalts (Ubide et al., 2019 and references therein), but has rarely been reported in cumulate rocks (Latypov et al., 2020). The formation and preservation of disequilibrium textures require fast crystal growth that exceeds lattice diffusion (Watson and Liang, 1995), processes most likely to occur in volcanic rocks. Here we report clear hourglass zoning of diopside and demonstrate a kinetic control on element distribution in the Mouding intrusion, which indicates that the growth rate of clinopyroxene cumulates can be fast and disequilibrium crystallization can also occur in plutonic rocks. We further note that elemental enrichment factors correlate positively with magmatic cooling rates (Fig. 9). Basalts with fine-grained or glassy groundmasses have the highest elemental enrichment slopes (Ubide et al., 2019), whereas those with holocrystalline groundmasses (Shimizu, 1981) have moderate slopes, and in this study, clinopyroxenite with granular textures have gentle slopes. A possible explanation is that higher cooling rates can lead to faster crystal growth and higher degrees of disequilibrium crystallization. This effect is more obvious for elements with higher Z/r^2, such as Nb, Ta, Ti, Zr, and Hf, than those with lower Z/r^2, such as Mn, Fe, Co, Mg, and Ni (Fig. 9). We propose that the hourglass zoning of clinopyroxene can provide valuable information on disequi-

Table 4
Crystal size distribution for clinopyroxenite and magnetite clinopyroxenite from the Mouding mafic–ultramafic intrusion.

Sample No.	Diopside volume (%)	Characteristic length	L max	Mean size	σ	Slope	σ	Intercept	σ
zk001-02	44.8	0.57	3.69	0.94	0.07	−1.75	0.04	1.93	0.06
zk001-05	45.0	0.53	4.84	0.89	0.06	−1.87	0.04	2.12	0.06
zk001-17	46.4	0.65	5.31	1.04	0.08	−1.54	0.04	1.38	0.07
zk001-29	54.8	0.78	6.03	1.34	0.12	−1.29	0.04	0.86	0.08
zk001-35	47.6	0.78	6.57	1.39	0.12	−1.28	0.04	0.62	0.09
zk001-43	49.6	0.99	6.71	1.65	0.19	−1.01	0.04	−0.12	0.11

librium mineral crystallization and magma cooling and suggest that this feature warrants more comprehensive investigation in the future.

6. CONCLUSIONS

Trace element mapping and EBSD analyses of euhedral diopside from the Mouding mafic–ultramafic intrusion provide new insights into the growth of clinopyroxene and Sc enrichment processes in mafic magmas. Together with crystal growth modelling, our results confirm that kinetic crystallization plays an important role in controlling the distribution of Sc in diopside and its concentration on prismatic faces. The CSD patterns of clinopyroxene indicate that textural coarsening dominates the nucleation and growth of clinopyroxene, favoring the formation of Sc-rich clinopyroxene. Relatively high volatile content and low magma viscosity are favorable for magma convection and diffusive transport of elements, which can exert pronounced influences on textural coarsening. We suggest that complex and irregular Sc distribution patterns of Sc-rich minerals documented in the literature are due not only to compositional variations of magmas, but also to significant kinetic effects. Kinetic crystallization can lead to simultaneous concentration of Sc and some HFSEs on certain crystal faces, thus caution is required when explaining their affinity. Element enrichment factors along different crystal faces may be positively correlated with magma cooling rates, which can provide valuable information about magma evolution.

7. RESEARCH DATA

This research includes 4 tables, 9 figures and 2 supplementary figures. Tables 1–4 and Figs. 1–9 are included in the manuscript. Two supplementary figures are attached with as Supplementary Material. All the research data for this paper are available at figshare data repository: https://doi.org/10.6084/m9.figshare.19096619.

Declaration of Competing Interest

The authors declare that they have no known competing financial interests or personal relationships that could have appeared to influence the work reported in this paper.

ACKNOWLEDGEMENTS

We thank Dr. Eric Dowty for guidance with the SHAPE software, Dr. Frankie Y.F. Chan for the EBSD analyses, Prof. Fang-Yue Wang for the LA-ICP-MS analyses, Ms. Xiao Fu for the EPMA analyses, Dr. Xiao-Liang Cui for the CSD analyses, and Prof. Ze-Rui Liu and Prof. Ya-Fei Wu for assistance with the field sampling. The authors are grateful to Jeffrey G. Catalano and Georges Calas for editorial handling, to Dr. Mathieu Chassé and two anonymous reviewers for their valuable comments and to Dr. Teresa Ubide for her constructive suggestion on an early version of the manuscript. This work was funded by the National Natural Science Foundation of China (91962216 and 41772087) to Mei-Fu Zhou and a Student Research Grant from the Hugh McKinstry Fund to Zhen-Chao Wang. Paul T. Robinson acknowledges receipt of an Open Fund Grant (No. GPMR201901) from China University of Geosciences, Wuhan.

APPENDIX A. SUPPLEMENTARY MATERIAL

Supplementary data to this article can be found online at https://doi.org/10.1016/j.gca.2022.03.016.

REFERENCES

Bédard J. H. (2014) Parameterizations of calcic clinopyroxene—Melt trace element partition coefficients. *Geochem. Geophys. Geosyst.* **15**(2), 303–336.

Cameron M., Sueno S., Prewitt C. T. and Papike J. J. (1973) High-temperature crystal chemistry of acmite, diopside, hedenbergite jadeite, spodumene and ureyite. *Am. Miner.* **58**, 594–618.

Chakhmouradian A. R., Smith M. P. and Kynicky J. (2015) From "strategic" tungsten to "green" neodymium: A century of critical metals at a glance. *Ore Geol. Rev.* **64**, 455–458.

Chassé M., Griffin W. L., O'Reilly S. Y. and Calas G. (2017) Scandium speciation in a world- class lateritic deposit. *Geochem. Perspect. Lett.* **3**, 105–114.

Chassé M., Griffin W. L., Alard O., O'Reilly S. Y. and Calas G. (2018) Insights into the mantle geochemistry of scandium from a meta-analysis of garnet data. *Lithos* **310–311**, 409–421.

Chassé M., Griffin W. L., O'Reilly S. Y. and Calas G. (2019) Australian laterites reveal mechanisms governing scandium dynamics in the critical zone. *Geochim. Cosmochim. Acta* **260**, 292–310.

Cherniak D. J. and Liang Y. (2007) Rare earth element diffusion in natural enstatite. *Geochim. Cosmochim. Acta* **71**(5), 1324–1340.

Clark J. R., Appleman D. E. and Papike J. J. (1969) Crystal-chemical characterization of clinopyroxenes based on eight new structure refinements. *Miner. Soc. Am. Spec. Pap.* **2**, 31–50.

Cook N., Ciobanu C. L., George L., Zhu Z. Y., Wade B. and Ehrig K. (2016) Trace element analysis of minerals in magmatic-hydrothermal ores by laser ablation inductively-coupled plasma mass spectrometry: Approaches and opportunities. *Minerals* **6**, 111.

Čopjaková R., Škoda R., Galiová M. V., Novák M. and Cempírek J. (2015) Sc-and REE-rich tourmaline replaced by Sc-rich REE-bearing epidote-group mineral from the mixed (NYF+ LCT) Kracovice pegmatite (Moldanubian Zone, Czech Republic). *Am. Miner.* **100**, 1434–1451.

Daigle P. J. (2017) NI 43–101 technical report on the crater Lake Sc-Nb-REE project Québec, Canada. In *Prepared for: peak mining corporation, NQ exploration Inc and Imperial Mining Group Ltd P. Daigle consulting services*, pp. 1–68.

DeHoff R. T. (1991) A geometrically general theory of diffusion controlled coarsening. *Acta Metall. Mater.* **39**(10), 2349–2360.

Dowty E. (1976) Crystal structure and crystal growth; II, Sector zoning in minerals. *Am. Miner.* **61**, 460–469.

Dowty E. R. I. C. (1980) Computing and drawing crystal shapes. *Am. Miner.* **65**(5–6), 465–471.

Dowty, E.R.I.C., 1987. SHAPE Copyright 1994, Shape Software 521 Hidden Valley Road, Kingsport, TN 37663, USA. http://www.shapesoftware.com.

Eby G. N. (1973) Scandium geochemistry of the Oka carbonatite complex, Oka, Quebec. *Am. Miner.* **58**(9–10), 819–825.

Foord E. E., Birmingham S. D., Demartin F., Pilati T., Gramaccioli C. M. and Lichte F. E. (1993) Thortveitite and associated Sc-bearing minerals from Ravalli County, Montana. *Can. Mineral.* **31**(2), 337–346.

Fu Y., Wang S., Sun X., Liao Z., Jiang X., Ren G., Zhou B., Guo Y. and Wang Z. (2015) LA-ICP-MS zircon U-Pb age and petrogeochemical features of Huangguayuan Granite, Yuanmou, Yunnan Province and its geological implication. *Geol. Rev.* **61**, 376–392, in Chinese with English abstract.

Gao Y., Hoefs J., Hellebrand E., von der Handt A. and Snow J. E. (2007) Trace element zoning in pyroxenes from ODP Hole 735B gabbros: diffusive exchange or synkinematic crystal fractionation?. *Contrib. Mineral. Petrol.* **153**(4), 429–442.

Gramaccioli C. M., Diella V. and Demartin F. (2000) The formation of scandium minerals as an example of the role of complexes in the geochemistry of rare earths and HFS elements. *Eur. J. Mineral.* **12**(4), 795–808.

Groth, P., Krantz, F., 1880. The P. Groth & F. Krantz collection of 743 crystal models.

Guo Y. S., Zeng P. S., Guo X., Cui Y. L., Yang X. S., Lu W. J., Guo Q. and Yang Z. L. (2012) Some problems concerning scandium and scandium-bearing potential of the mafic-ultramafic intrusions in central Yunnan Province. *Acta Geosci. Sin.* **33**(5), 745–754, in Chinese with English abstract.

Halkoaho T., Ahven M., Rämö O. T., Hokka J. and Huhma H. (2020) Petrography, geochemistry, and geochronology of the Sc-enriched Kiviniemi ferrodiorite intrusion, eastern Finland. *Miner. Depos.* **55**, 1561–1580.

Higgins M. D. (1998) Origin of anorthosite by textural coarsening: quantitative measurements of a natural sequence of textural development. *J. Petrol.* **39**, 1307–1323.

Higgins M. D. (2000) Measurement of crystal size distributions. *Am. Miner.* **85**(9), 1105–1116.

Higgins M. D. (2002) A crystal size-distribution study of the Kiglapait layered mafic intrusion, Labrador, Canada: evidence for textural coarsening. *Contrib. Mineral. Petrol.* **144**, 314–330.

Kalashnikov A. O., Yakovenchuk V. N., Pakhomovsky Y. A., Bazai A. V., Sokharev V. A., Konopleva N. G., Mikhailova J. A., Goryainov P. M. and Ivanyuk G. Y. (2016) Scandium of the Kovdor baddeleyite–apatite–magnetite deposit (Murmansk Region, Russia): Mineralogy, spatial distribution, and potential resource. *Ore Geol. Rev.* **72**, 532–537.

Kempe U. and Wolf D. (2006) Anomalously high Sc contents in ore minerals from Sn–W deposits: possible economic significance and genetic implications. *Ore Geol. Rev.* **28**, 103–122.

Latypov R. M., Chistyakova S. Y., Namur O. and Barnes S. (2020) Dynamics of evolving magma chambers: textural and chemical evolution of cumulates at the arrival of new liquidus phases. *Earth Sci. Rev.* **210**, 103388.

Li X., Zeng Z., Yang H., Zhao Y., Yin X., Wang X., Chen S., Qi H. and Guo K. (2020) Integrated major and trace element study of clinopyroxene in basic, intermediate and acidic volcanic rocks from the middle Okinawa Trough: Insights into petrogenesis and the influence of subduction component. *Lithos* **352**, 105320.

Liferovich R. P., Subbotin V. V., Pakhomovsky Y. A. and Lyalina M. F. (1998) A new type of scandium mineralization in phoscorites and carbonatites of the Kovdor massif, Russia. *Can. Mineral.* **36**(4), 971–980.

Liu Y. S., Hu Z. C., Gao S., Günther D., Xu J., Gao C. G. and Chen H. H. (2008) In situ analysis of major and trace elements of anhydrous minerals by LA-ICP-MS without applying an internal standard. *Chem. Geol.* **257**, 34–43.

Marsh B. D. (1988) Crystal size distribution (CSD) in rocks and the kinetics and dynamics of crystallization. *Contrib. Mineral. Petrol.* **99**, 277–291.

Masotta M., Pontesilli A., Mollo S., Armienti P., Ubide T., Nazzari M. and Scarlato P. (2020) The role of undercooling during clinopyroxene growth in trachybasaltic magmas: Insights on magma decompression and cooling at Mt. Etna volcano. *Geochim. Cosmochim. Acta* **268**, 258–276.

Mattsson H. B. and Caricchi L. (2009) Experimental constraints on the crystallization of natrocarbonatitic lava flows. *Bull. Volcanol.* **71**, 1179–1193.

McCarron T., Gaidies F., McFarlane C. R., Easton R. M. and Jones P. (2014) Coupling thermodynamic modeling and high-resolution in situ LA-ICP-MS monazite geochronology: evidence for Barrovian metamorphism late in the Grenvillian history of southeastern Ontario. *Mineral. Petrol.* **108**, 741–758.

Momma K. and Izumi F. (2011) VESTA 3 for three-dimensional visualization of crystal, volumetric and morphology data. *J. Appl. Crystallogr.* **44**(6), 1272–1276.

Morgan D. J. and Jerram D. A. (2006) On estimating crystal shape for crystal size distribution analysis. *J. Volcanol. Geotherm. Res.* **154**(1–2), 1–7.

Nakamura Y. (1973) Origin of sector-zoning of igneous clinopyroxenes. *Am. Miner.* **58**, 986–990.

Nazzareni S., Skogby H. and Halenius U. (2013) Crystal chemistry of Sc-bearing synthetic diopsides. *Phys. Chem. Miner.* **40**, 789–798.

Petrus J. A., Chew D. M., Leybourne M. I. and Kamber B. S. (2017) A new approach to laser-ablation inductively-coupled-plasma mass-spectrometry (LA-ICP-MS) using the flexible map interrogation tool 'Monocle'. *Chem. Geol.* **463**, 76–93.

Samson I. M. and Chassé M. (2016) Scandium. In *Encyclopedia of Geochemistry A Comprehensive Reference Source on the Chemistry of the Earth* (eds. W. M. White, W. H. Casey, B. Marty and H. Yurimoto). Springer International Publishing AG, Switzerland, pp. 1323–1326.

Schneider C. A., Rasband W. S. and Eliceiri K. W. (2012) NIH Image to ImageJ: 25 years of image analysis. *Nat. Methods* **9**(7), 671–675.

Shannon R. D. (1976) Revised effective ionic radii and systematic studies of interatomic distances in halides and chalcogenides. *Acta Crystallogr. Sec. A* **32**, 751–767.

Shimizu N. (1981) Trace element incorporation into growing augite phenocryst. *Nature* **289**, 575–577.

Sun C. (2021) Trace element geothermometry and geospeedometry for cumulate rocks: Quantitative constraints on thermal and magmatic processes during igneous crust formation. In *Crustal Magmatic System Evolution: Anatomy, Architecture, and Physico-Chemical Processes* (eds. M. Masotta, C. Beier and S. Mollo). American Geophysical Union, pp. 19–43.

Tang Q., Zhang M., Wang Y., Yao Y., Du L., Chen L. and Li Z. (2017) The origin of the Zhubu mafic-ultramafic intrusion of the Emeishan large igneous province, SW China: Insights from volatile compositions and C-Hf-Sr-Nd isotopes. *Chem. Geol.* **469**, 47–59.

Tecchiato V., Gaeta M., Mollo S., Bachmann O., von Quadt A. and Scarlato P. (2018) Snapshots of primitive arc magma evolution recorded by clinopyroxene textural and compositional variations: The case of hybrid crystal-rich enclaves from Capo Marargiu Volcanic District (Sardinia, Italy). *Am. Miner.* **103**(6), 899–910.

Tong X., Liu Y., Hu Z., Chen H., Zhou L., Hu Q., Xu R., Deng L., Chen C., Yang L. and Gao S. (2016) Accurate determination of Sr isotopic compositions in clinopyroxene and silicate glasses by LA-MC-ICP-MS. *Geostand. Geoanal. Res.* **40**(1), 85–99.

Ubide T., McKenna C. A., Chew D. M. and Kamber B. S. (2015) High-resolution LA-ICP-MS trace element mapping of igneous minerals: In search of magma histories. *Chem. Geol.* **409**, 157–168.

Ubide T., Mollo S., Zhao J. X., Nazzari M. and Scarlato P. (2019) Sector-zoned clinopyroxene as a recorder of magma history,

eruption triggers, and ascent rates. *Geochim. Cosmochim. Acta* **251**, 265–283.

Wang F. Y., Ge C., Ning S. Y., Nie L. Q., Zhong G. X. and White N. C. (2017) A new approach to LA-ICP-MS mapping and application in geology. *Acta Petrol. Sin.* **33**(11), 3422–3436, in Chinese with English abstract.

Wang M. and Wang C. Y. (2020) Crystal Size Distributions and Trace Element Compositions of the Fluorapatite from the Bijigou Fe–Ti Oxide-Bearing Layered Intrusion, Central China: Insights for the Expulsion Processes of Interstitial Liquid from Crystal Mush. *J. Petrol.* **61**, egaa069.

Wang Y., Fan W., Zhang G. and Zhang Y. (2013) Phanerozoic tectonics of the South China Block: key observations and controversies. *Gondwana Res.* **23**(4), 1273–1305.

Wang Z., Li M. Y. H., Liu Z. R. R. and Zhou M. F. (2021) Scandium: ore deposits, the pivotal role of magmatic enrichment and future exploration. *Ore Geol. Rev.* **128**, 103906.

Watson E. B. and Liang Y. (1995) A simple model for sector zoning in slowly grown crystals: Implications for growth rate and lattice diffusion, with emphasis on accessory minerals in crustal rocks. *Am. Miner.* **80**(11–12), 1179–1187.

Wedepohl K. H. (1995) The composition of the continental crust. *Geochim. Cosmochim. Acta* **59**, 1217–1232.

Welsch B., Hammer J., Baronnet A., Jacob S., Hellebrand E. and Sinton J. (2016) Clinopyroxene in postshield Haleakala ankaramite: 2. Texture, compositional zoning and supersaturation in the magma. *Contrib. Mineral. Petrol.* **171**, 6.

Williams-Jones A. E. and Vasyukova O. V. (2018) The economic geology of scandium, the runt of the rare earth element litter. *Econ. Geol.* **113**, 973–988.

Wise M. A., Cerny P. and Falster A. U. (1998) Scandium substitution in columbite-group minerals and ixiolite. *Can. Mineral.* **36**(2), 673–680.

Wu Y. F., Fougerouse D., Evans K., Reddy S. M., Saxey D. W., Guagliardo P. and Li J. W. (2019) Gold, arsenic, and copper zoning in pyrite: A record of fluid chemistry and growth kinetics. *Geology* **47**(7), 641–644.

Xia F., Brugger J., Chen G., Ngothai Y., O'Neill B., Putnis A. and Pring A. (2009) Mechanism and kinetics of pseudomorphic mineral replacement reactions: A case study of the replacement of pentlandite by violarite. *Geochim. Cosmochim. Acta* **73**(7), 1945–1969.

Yu S. Y., Song X. Y., Chen L. M. and Li X. B. (2014) Postdated melting of subcontinental lithospheric mantle by the Emeishan mantle plume: Evidence from the Anyi intrusion, Yunnan, SW China. *Ore Geol. Rev.* **57**, 560–573.

Zhang B., Hu X., Asimow P. D., Zhang X., Xu J., Fan D. and Zhou W. (2019) Crystal size distribution of amphibole grown from hydrous basaltic melt at 0.6–2.6 GPa and 860–970 C. *Am. Miner.* **104**, 525–535.

Zhang W., Hu Z. and Liu Y. (2020) Iso-Compass: new freeware software for isotopic data reduction of LA-MC-ICP-MS. *J. Anal. At. Spectrom.* **35**(6), 1087–1096.

Zhang Z., Mahoney J. J., Mao J. and Wang F. (2006) Geochemistry of picritic and associated basalt flows of the western Emeishan flood basalt province, China. *J. Petrol.* **47** (10), 1997–2019.

Zhang Z., Mao J., Saunders A. D., Ai Y., Li Y. and Zhao L. (2009) Petrogenetic modeling of three mafic–ultramafic layered intrusions in the Emeishan large igneous province, SW China, based on isotopic and bulk chemical constraints. *Lithos* **113**(3–4), 369–392.

Zhao G. C. and Cawood P. A. (2012) Precambrian geology of China. *Precambr. Res.* **222–223**, 13–54.

Zhou M. F., Chen W. T., Wang C. Y., Prevec S. A., Liu P. P. and Howarth G. G. (2013) Two stages of immiscible liquid separation in the formation of Panzhihua-type Fe-Ti-V oxide deposits, SW China. *Geosci. Front.* **4**, 481–502.

Zhu Z. H. (2010) The discovery and significance of Sc in Ertaipo rock body of Mouding, Yunnan. *Yunnan Geol.* **29**, 235–244, in Chinese with English abstract.

Associate editor: Georges Calas